



1 **Assessing the degree of plug flow in oxidation flow reactors (OFRs): a study on a Potential**  
2 **Aerosol Mass (PAM) reactor**

3

4 Dhruv Mitroo<sup>1,a,\*</sup>, Yujian Sun<sup>1,\*</sup>, Daniel P. Combest<sup>2</sup>, Purushottam Kumar<sup>3</sup>, and Brent J.  
5 Williams<sup>1</sup>

6

7 <sup>1</sup>Department of Energy, Environmental & Chemical Engineering, Washington University in St.  
8 Louis, St. Louis, MO, USA

9

<sup>2</sup>ENGYS, Ltd.

10 <sup>3</sup>Discipline of Chemical Engineering, Indian Institute of Technology Gandhinagar, Palaj, Gujarat  
11 382355, India

12

13 <sup>a</sup>Now at the Department of Atmospheric Sciences, Rosenstiel School of Marine and Atmospheric  
14 Sciences, University of Miami, Miami, FL, USA

15

16 \*equally contributing authors

17

18 Correspondence to: [brentw@wustl.edu](mailto:brentw@wustl.edu)

19

Brent J. Williams, Ph.D.

20

Raymond R. Tucker I-CARES Career Development Associate Professor

21

Department of Energy, Environmental & Chemical Engineering

22

Washington University in St. Louis

23



24 **Abstract**

25

26 Oxidation flow reactors (OFRs) have been developed to achieve high degrees of oxidant exposures  
27 over relatively short space times (defined as the ratio of reactor volume to the volumetric flowrate).  
28 While, due to their increased use, attention has been paid to their ability to replicate realistic  
29 tropospheric reactions by modeling the chemistry inside the reactor, there is a desire to customize  
30 flow patterns. This work demonstrates the importance of decoupling tracer signal of the reactor  
31 from that of the tubing when experimentally obtaining these flow patterns. We modeled the  
32 residence time distributions (RTDs) inside the Washington University Potential Aerosol Mass  
33 (WU-PAM) reactor, an OFR, for a simple set of configurations by applying the tank-in-series (TIS)  
34 model, a one parameter model, to a deconvolution algorithm. The value of the parameter,  $N$ , is  
35 close to unity for every case except one having the highest space time. Combined, the results  
36 suggest that volumetric flowrate affects mixing patterns more than use of our internals. We  
37 selected results from the simplest case, at 78s space time with one inlet and one outlet, absent of  
38 baffles and spargers, and compared the experimental F-Curve to that of a computational fluid  
39 dynamics (CFD) simulation. The F-Curves, which represents the cumulative time spent in the  
40 reactor by flowing material, match reasonably well. We value that the use of a small aspect ratio  
41 reactor such as the WU-PAM reduces wall interactions, and suggest applying the methodology of  
42 tracer testing described in this work to investigate RTDs in OFRs and modify inlets, outlets, and  
43 use of internals prior to applications (e.g., field deployment vs. laboratory study).

44

45 **1 Introduction**

46



47 Tubular reactors were first introduced to the field of atmospheric science by means of small flow  
48 cell reactors developed to study the kinetics of stratospheric reactions (Brune et al., 1983; Howard,  
49 1979; Keyser, 1980; Lamb et al., 1983). Accurate kinetic measurements were possible due to the  
50 high pipe aspect ratios, which encouraged a high degree of plug flow behavior (Keyser, 1984).  
51 The design of these miniature tubular reactors, with volumes on the order of a few cm<sup>3</sup>, was  
52 different from that of significantly larger, batch-type or semi-continuous type well mixed reactors,  
53 with volumes on the order of several m<sup>3</sup>, built to understand aerosol formation in the troposphere  
54 (Crump et al., 1982; Crump and Seinfeld, 1980; Leone et al., 1985). To study aerosol formation  
55 and growth chemistry, the dynamics of atmospheric circulation and transport needed to be  
56 excluded. It was therefore convenient to mimic the troposphere by treating it as an enormous, well  
57 mixed reactor, which led to the development of larger well mixed reactors. The discovery of  
58 secondary processes preceding aerosol formation led to significant emphasis on the study of  
59 secondary organic aerosol (SOA) formation (Haagen-Smit, 1952, 1963, 1970; Went, 1960). The  
60 approach of using large, well mixed batch-style environmental chambers eventually helped  
61 elucidate chemical mechanisms for model compounds (Claeys, 2004; Kamens et al., 1982; Kroll  
62 et al., 2006; Nozière et al., 1999; Paulson et al., 1990; Pereira et al., 2015; Volkamer et al., 2001),  
63 and, with improved instrumentation (Canagaratna et al., 2007; Crouse et al., 2006; de Gouw and  
64 Warneke, 2007; Hansel et al., 1995; Jayne et al., 2000; Williams et al., 2006; Zhao et al., 2013),  
65 the community gained a better understanding of SOA formation. Unfortunately, low levels of  
66 conversion and high wall losses seen in these large reactors did not allow simulated exposures that  
67 exceeded a day at most, which is just a short glimpse into the average two week lifespan of an  
68 atmospheric aerosol (Seinfeld and Pandis, 2006). Due to such limitations, oxidation flow reactors  
69 (OFRs) with short spacetimes (ratio of reactor volume to the volumetric flowrate) are being



70 developed (Cazorla and Brune, 2010; Ezell et al., 2010; George et al., 2007; Huang et al., 2016;  
71 Kang et al., 2007).

72

73 OFRs can be viewed as tubular reactors due to their pipe aspect. They have been widely used for  
74 over a decade to study heterogeneous reactions on organic aerosol surfaces involving gas-phase  
75 oxidants such as hydroxyl radicals and ozone (George et al., 2007; George and Abbatt, 2010;  
76 Katrib et al., 2005; Kessler et al., 2010, 2012; Knopf et al., 2005; Kroll et al., 2012; Smith et al.,  
77 2009). These reactors are able to generate very high concentrations of hydroxyl (OH) radicals, tens  
78 to thousands times higher than typical tropospheric levels, which accelerates the rate of gas-phase  
79 oxidation reactions. Within spacetimes of a few minutes, it is possible to achieve integrated oxidant  
80 exposures equivalent to multiple days or weeks of atmospheric oxidation. It is important to  
81 distinguish OFRs from modern day conventional flow tube reactors, which stem from designs of  
82 old flow tube reactors (e.g., Keyser 1984) but employed in the study of gas uptake kinetics on  
83 aerosol surfaces rather than homogeneous gas-phase reactions, as described in the previous  
84 paragraph. Beyond the original application of heterogeneous oxidation studies, Kang et al.  
85 introduced the potential aerosol mass (PAM) OFR which, alongside newer OFR designs, was  
86 intended specifically for studies of SOA physicochemical properties (Kang et al., 2007, 2011;  
87 Keller and Burtscher, 2012; Lambe et al., 2011b, 2012, 2013; Massoli et al., 2010; Ortega et al.,  
88 2013; Slowik et al., 2012). This application therefore altered the study of SOA formation,  
89 previously dominated by the traditional large, well mixed reactors (Kroll and Seinfeld, 2008;  
90 Rudich et al., 2007; Turpin et al., 2000), by allowing to generate laboratory data beyond first  
91 simulated day of exposure. Because the mechanism of exposure between traditional chambers  
92 OFRs was different, validating the OFR concept began by replicating data obtained from



93 traditional chambers (Chhabra et al., 2015; Lambe et al., 2015; Liu et al., 2015), and to assess  
94 whether the chemistry was realistic (Li et al., 2015; McNeill et al., 2008; Peng et al., 2015;  
95 Renbaum and Smith, 2011). Consequently, much modeling work has focused on pure chemical  
96 reactions and comparison of SOA yields between the two (Bruns et al., 2015; Lambe et al., 2015;  
97 Li et al., 2015; Ortega et al., 2015; Peng et al., 2015). However, essentially no modeling work has  
98 been done on understanding hydrodynamics or flow fields inside OFRs so that the flow patterns  
99 can be improved. In a study from Li et al., it appears that residence time distributions (RTDs) that  
100 deviate significantly from plug flow in the PAM result only in a ~10% error of reported values  
101 such as OH exposure (Li et al., 2015), which is conducive to OFRs being viewed as tubular  
102 reactors. It is unknown if the error may trend with external OH reactivity ( $\text{OHR}_{\text{ext}}$ ) and become  
103 more significant for slow reacting compounds, although efforts by the Jimenez Group at the  
104 University of Colorado at Boulder are underway.

105

106 In both single and multiphase reactors, contact patterns and the degree of mixing determine reactor  
107 performance, e.g., selectivity and yield (Bourne, 2003; Deckwer, 1976; Levenspiel, 1999). This  
108 implies that upon desired contacting, chemical pathways that would be otherwise suppressed can  
109 become more competitive. For example, if during a mixed OH / ozonolysis heterogeneous  
110 reaction, a fresh biomass burning aerosol is introduced in the centerline port of an OFR and ozone  
111 is introduced along a side port, most of the aerosol may travel ballistically through the chamber  
112 having limited contact with ozone or OH, and chemical reaction is less competitive with photolysis  
113 / photobleaching reactions of the aerosol. RTDs describe the probability of a fluid element's age  
114 inside the reactor: one can think of those as the probability distribution function (PDF) of a fluid  
115 element in the reactor (Fogler, 2006; Levenspiel, 1999). Tools are available to diagnose or predict



116 flow behavior. These tools fall in two categories: tracer tests (diagnostics) and computational fluid  
117 dynamics (CFD) simulations (predictions).

118

119 We present a technique to assess the degree of plug flow in an OFR, that can be in principle  
120 extended to any vessel. The rigor of the technique is tested by varying use of internals and flowrate  
121 and observing the resulting RTD curves in the Washington University PAM (WU-PAM) reactor.  
122 We begin by introducing an experimental method for obtaining the reactor RTD, which can be  
123 applied to any other OFR, via inert tracer injections. From raw data, we explain how to obtain  
124 PDFs. We chose to run CFD on the simplest design (a base case configuration) of the WU-PAM  
125 reactor to gain hydrodynamics information. Finally, we compare results from tracer tests and CFD  
126 for the base case. We compare this approach to that of previous studies by Lambe et al. (Lambe et  
127 al., 2011a), Huang et al. (Huang et al., 2016), and Simonen et al. (Simonen et al., 2016), to the best  
128 of our knowledge, the only other studies on RTDs in OFRs. We do not provide predictive  
129 configurations for the PAM reactor because there are many avenues different groups can take  
130 depending on their focus, and this study is central to the current design.

131

## 132 **2 Methods**

133

134 The WU-PAM reactor is an iridite-treated aluminum cylinder, 18 inches in length and 8 inches in  
135 inner diameter, giving it a total volume of 13 L. It has two 12 inch mercury lamps with peak  
136 wavelengths at 185 nm and 254 nm (BHK Inc. Analamp Model No. 82-9304-03) housed in Teflon  
137 sheaths, directly opposite each other, along the axial direction. Annular flow of N<sub>2</sub> (Airgas)  
138 through the sheaths prevents direct contact with the lamps and purges any outgas products when



139 the lamps are turned on. The mercury lamps are left in place with their housing to mimic simple  
140 OFR internals; they have not been turned on during this study. Details of their mode of operations  
141 for oxidant formation can be found elsewhere (Li et al., 2015; Peng et al., 2015, 2016). OFRs like  
142 the WU-PAM have removable internals, face plates, and peripheral inlets and outlets that allow a  
143 wide variety of configurations. For example, Ortega et al. removed the inlet plate of their PAM  
144 reactor during a deployment in the Fire Lab at Missoula Experiment (FLAME-3) while keeping  
145 the inlet baffle to reduce particle loss, and in doing so observed a reduction in jetting of centerline  
146 flow (Ortega et al., 2013). In a different study, Lambe et al. ran experiments keeping the inlet plate  
147 on the PAM coupled with a sparger (a cap with large holes in the side in fixed onto the inlet, so  
148 that the flow does not jet into the chamber), because laboratory experiments required a closed  
149 system (Lambe et al., 2011a).

150

151 In this work, we chose four configurations: I (one inlet, one outlet, two lamp housings as internals),  
152 II (one inlet, one outlet, two lamp housings with sparger and baffles as internals), III (multiple  
153 inlets, multiple outlets, two lamp housings as internals), and IV (multiple inlets, one outlet, two  
154 lamp housings with sparger and baffles as internals). Configuration I at 78s spacetime was subject  
155 to a CFD simulation as a simple scenario where the simulation could capture hydrodynamics  
156 accurately.

157

## 158 **2.1 Tracer studies**

159

160 The laboratory setup to determine RTDs experimentally is shown in Fig. 1. N<sub>2</sub> (Airgas) was the  
161 carrier fluid and SO<sub>2</sub> (Air Liquide) was the inert tracer. Both flow rates were controlled by mass



162 flow controllers (MFCs) (Pneucleus Technologies, LLC). All experiments began by allowing one  
163 hour to achieve a steady state of the carrier gas' flow profile inside the reactor, after which SO<sub>2</sub>  
164 was introduced in a single step-up manner. A tracer flowrate of 100 cm<sup>3</sup> min<sup>-1</sup> allowed good  
165 detection in the measurement and minimized perturbation of the flow field. Analogously, the flow  
166 of the carrier fluid was stepped down to maintain a constant desired total volumetric flowrate. SO<sub>2</sub>  
167 mixing ratios were determined by a Trace level-Enhanced SO<sub>2</sub> Analyzer (Thermo Scientific Model  
168 43i, Thermo Scientific) via pulsed fluorescence, and the instrument was set to an averaging time  
169 of 10s. This setting was the highest frequency over which the instrument could average the signal.  
170 Obtaining high frequency data simplifies data analysis by avoiding the need for interpolation  
171 techniques, as discussed in Sect. S1.

172

173 We expected that the tracer would experience an associated spacetime and RTD in places other  
174 than the reactor, between the exit of the flow controller and the SO<sub>2</sub> detection chamber in the gas  
175 analyzer. We therefore ran two experiments for every WU-PAM reactor configuration. The first  
176 incorporated both the reactor and the inlet and outlet plumbing, and the second bypassed the  
177 reactor. From these two signals we could extract the actual reactor RTD as described in Sect. 3.2.  
178 Both experiments were operated by allowing the formation of fully developed flow before  
179 injecting the tracer stepwise, as mentioned previously. Appendix A describes in detail how we  
180 obtained a PDF and a cumulative distribution function (CDF) from raw data.

181

182 The WU-PAM reactor has peripheral inlets and outlets to optionally create allow a ring (annular)  
183 flow around the centerline. Ideally, a uniformly distributed flow around the centerline helps  
184 stabilize the flow, avoids recirculation, and reduces wall losses. To create ring flow, we formed a





185 three-eighth inch Teflon tube into a circle, and drilled six one-sixteenth inch diameter holes evenly  
186 spaced along the side of the tube facing in the direction of flow. A similar Teflon tube circle was  
187 created for the outflow. The ring flow setup required additional plumbing internals (Fig. 1b).  
188 Tracer tests were accomplished for configuration I at three different spacetimes ( of 52s, 78s, and  
189 152s), for three different configurations ( I, II, and III) at a 78s spacetime, and an arbitrary special  
190 case for configuration IV at 411 s spacetime (configuration and spacetime not commonly used).

191

## 192 **2.2 Simulations**

193

194 While tracer studies are a powerful diagnostic tool and result, if done correctly, in accurate RTDs,  
195 they cannot capture the full hydrodynamics details, or the state of mixing in the reactor (i.e., the  
196 exchange of mass between the fluid elements). Both hydrodynamics and mixing can significantly  
197 influence the reactor performance (Fogler, 2006; Villiermaux, 1986). For configuration I at 78s  
198 spacetime, we ran a CFD simulation to visualize the hydrodynamics inside the WU-PAM. This  
199 comparative analysis seeks to provide validation prior to using the CFD platform as a predictive  
200 tool for mixing patterns in OFRs with more complex geometry or internals.

201

202 As a solver, we used OpenFOAM, an open source CFD toolbox available at [www.openfoam.com](http://www.openfoam.com)  
203 or [www.openfoam.org](http://www.openfoam.org). The reactor geometries were constructed on FreeCAD, an open source  
204 computer aided design (CAD) software available at [www.freecadweb.org](http://www.freecadweb.org), and Onshape, available  
205 at [www.onshape.com](http://www.onshape.com), prior to being exported into OpenFOAM. To discretize the volume elements  
206 in the geometry, a mesh was created using the snappyHexMesh tool in OpenFOAM either directly  
207 or in the HELYX-OS GUI. By generating mainly hexahedral meshes, this tool can mesh objects



208 of irregular shape. Then, additional layers of different geometry are added to the surface to improve  
209 the mesh quality. A figure and details of the mesh can be found in Figure S1 and Table S1,  
210 respectively. The hydrodynamics were calculated using simpleFoam, a steady-state solver for  
211 single phase incompressible laminar or turbulent flow. We used first order schemes, and specified  
212 the boundary conditions in each simulation case. The outlets had zero gradient for velocity and  
213 fixed values for pressure, while the walls had fixed value for velocity and zero gradient for  
214 pressure. After the flow field is obtained, a tracer experiment is simulated by scalarTransportFoam  
215 for one of the simulations, which solves the transient convection-diffusion transport equation of a  
216 passive scalar (dimensionless tracer concentration in this case). The initial condition is zero  
217 concentration, and the boundary condition at the inlet is that the dimensionless tracer concentration  
218 is equal to 1. After the simulation, the exit concentration is mixing-cup averaged to output an F-  
219 Curve. We added a modification to the existing solver to account for turbulent diffusivity, which  
220 had a non-negligible effect on mixing in the WU-PAM reactor, particularly at the entrance jet for  
221 high flowrates. We found that the turbulent diffusivity was on the same order of magnitude as the  
222 molecular diffusivity within the jet region near the inlet, suggesting turbulence in the jet was  
223 significant. It is worthwhile to note that the inlet sparger and baffles (i.e., internals present in  
224 configuration II and IV) left out of the simulation could significantly affect this outcome, however  
225 those simulations required significant computer time to resolve mesh sizing.

226

### 227 **3 Results**

228

#### 229 **3.1 The RTD function, $E(t)$ , and the cumulative RTD function, $F(t)$**

230



231 Tracer tests give us fast qualitative information about the reactor, but mathematical manipulation  
232 (e.g., normalizing the data and scaling the axes) of the data provide quantitative information and  
233 offers a basis for comparing reactor behaviors on a universal scale. The main mathematical  
234 descriptors of a fluid element residing in a chamber are its PDF and its CDF. For a chemical  
235 reactor, the PDF is more commonly referred to as the RTD function,  $E(t)$ , in the dimensional  
236 domain, or  $E(\theta)$  in the dimensionless domain (referred to as E-Curves). Similarly, the CDF is  
237 called the cumulative RTD function,  $F(t)$ , in the dimensional domain, or  $F(\theta)$  in the  
238 dimensionless domain (referred to as F-Curves) (Danckwerts, 1953; MacMullin and Weber Jr.,  
239 1935). The relations between E-Curves and F-Curves are derived for the reader in this Appendix  
240 A, but are well established and available on the internet and in classical textbooks (Fogler, 2006;  
241 Levenspiel, 1999, 2002).

242

243 Figure 2 gives an example of how mathematical processing of the data looks. The shape of the  
244 curve does not change, but the axes do. Section S1 explains how we obtained a pulse response  
245 equivalent of concentration data from stepwise addition of the tracer.

246

247 In the WU-PAM, advective flow should be the main form of transport (we do not consider  
248 convective effects due to thermal gradients from lamp activity in this work). Modeling real reactors  
249 can be challenging, but approximations are possible using ideal reactor concepts (Levenspiel,  
250 2002). The two most common examples of ideal reactors are the plug flow reactor (PFR), where  
251 the flow is perfectly plugged or piston-like, and the continuously stirred tank reactor (CSTR),  
252 where the flow is perfectly mixed. Mathematically, their E-Curves are represented by Equations  
253 1-4:



254

$$E_{PFR}(t) = \delta(t - \bar{t}) \quad (1)$$

$$E_{PFR}(\theta) = \delta(\theta - 1) \quad (2)$$

$$E_{CSTR}(t) = \frac{1}{\bar{t}} e^{-\frac{t}{\bar{t}}} \quad (3)$$

$$E_{CSTR}(\theta) = e^{-\theta}. \quad (4)$$

255

256 Examples of how RTDs look like based on compartmental modeling using both ideal reactors are  
257 available in chemical engineering textbooks (Fogler, 2006; Levenspiel, 1999) and, although not  
258 discussed here, a variety of phenomenological models can be applied to describe or compare  
259 OFRs. It is then open to interpretation whether the combination of ideal reactors chosen for an E-  
260 Curve (e.g., a PFR and CSTR in series, or two CSTRs in parallel) describes the hydrodynamics of  
261 the reactor as well. The RTD of an OFR should be obtained experimentally, if possible, before  
262 deciding what model to use to describe it. Development of a phenomenological model to describe  
263 the WU-PAM RTD is beyond the scope of this study, whose aim is to develop a robust  
264 methodology to assess degree of plug flow in any OFR, however is an avenue that should be  
265 pursued in the future. Given our current setup at Washington University, the true reactor RTD is  
266 impossible to measure accurately by a single tracer injection. The tubing length, pressure drop  
267 inside the filter holder upstream of the SO<sub>2</sub> detector, and location of the SO<sub>2</sub> detector have not  
268 been minimized, thus we expect that collectively they could perturb our measurements  
269 significantly. We choose not to simply subtract the theoretical space time of the tubing, because  
270 non-ideal tracer injection or detection are most likely not represented by a Dirac function of a  
271 perfect impulse (or derived from a perfect stepwise injection, represented by the Heaviside



272 function). Therefore we need to deconvolute the RTD signal due to the reactor from the signal due  
273 to additional plumbing.

274

### 275 **3.2 Tank-in-Series model for indirect deconvolution**

276

277 Levenspiel describes the convolution integral (Levenspiel, 1999) in his textbook “Chemical  
278 Reaction Engineering”, which has been adapted to solve previous problems of decoupling RTD  
279 signals (Hamed, 2012; Han, 2007; Mills and Duduković, 1988; Simonen et al., 2016; Sun, 2010).

280 This integral focuses on packets of the tracer that enter  $t'$  seconds before  $t$ , that is  $(t - t')$ , and  
281 stay  $t'$  seconds in the reactor:

$$C_{out}(t) = \int_0^t C_{in}(t') \cdot E(t - t') dt', \quad (5)$$

282 or

$$C_{out}(t) = C_{in} * E \quad (6)$$

283 where  $E$  is the true E-Curve of the reactor, and  $C_{in}$  and  $C_{out}$  are the time-dependent concentration  
284 profiles of the measured tracer at the injection port and outlet port respectively. This equation is  
285 based on assumptions of mass conservation (i.e., no wall loss inside the reactor) and memory loss  
286 (i.e., the fluid elements in fast-moving fluid in a region are not bound to behave as fast-moving in  
287 another region). We separate two regions in our setup, and identify three E-Curves. These  
288 correspond to curves for the reactor, the plumbing (including filters, instrument plumbing, and the  
289 instrument detector chamber), and the two together. Respectively, we denote them as  $E_0(t)$ ,  $E_1(t)$ ,  
290 and  $E_2(t)$ . We are able to accurately measure  $E_2(t)$  and  $E_1(t)$ , but not  $E_0(t)$ . Thus, Eq. (6) now  
291 takes the form

$$E_2(t) = E_0(t) * E_1(t), \quad (7)$$



292 and we need to solve for  $E_0(t)$ . Details of the deconvolution approach can be found in Appendix  
293 B, however direct application of this technique failed to get the solution to converge. It is a robust  
294 protocol to accurately determine a numerical RTD, and should be applied whenever a stable  
295 solution is available.

296

297 What we propose is an indirect application, i.e., to guess  $E_0(t)$  so that the convolution integral  
298 yields a curve that matches that of  $E_2(t)$ . This requires a formidable number of guesses and  
299 iterations and could be a lengthy process if done numerically. One workaround is to assume a form  
300 of  $E_0(t)$ , ideally with one variable parameter, that can be tuned to give the  $E_2(t)$  that best matches  
301 the experimental  $E_2(t)$  curve. The CSTR and PFR forms should not be considered since they are  
302 ideal extremes of reactor behavior. We chose to apply the tank-in-series (TIS) model (MacMullin  
303 and Weber Jr., 1935) to the convolution integral since it is a one parameter model that, although  
304 not specific to flowtube, tubular, laminar, or plug-flow reactors, gives an idea of where the reactor  
305 lies on the spectrum of mixed flow vs. plugged flow based on the value of a parameter,  $N$ .  $N$  refers  
306 to the fictitious number of equivalent CSTRs that, in series, describe the E-Curve for the reactor.  
307 This function is

308

$$E(t) = \frac{t^{N-1}}{(N-1)! \left(\frac{\bar{t}}{N}\right)^N} e^{-\left(\frac{N}{\bar{t}}\right)t} \quad (8)$$

$$E(\theta) = \frac{N(N\theta)^{N-1}}{(N-1)!} e^{-N\theta}. \quad (9)$$

309



310 For a value of  $N = 1$ , the E-Curve becomes that of a perfect CSTR; for a value of  $N = \text{infinity}$ , it  
311 becomes that of a perfect PFR, as shown in Fig. S2. Using this model, the convolution integral  
312 takes the form

$$E_2^*(t) = \int_0^t E_1(t-t') \cdot \frac{t'^{N-1}}{(N-1)! \left(\frac{t}{N}\right)^N} e^{-\left(\frac{N}{t}\right)t'} dt', \quad (10)$$

313 where  $E_1(t-t')$  is an array of accurate experimental data already obtained, and  $E_2^*(t)$  is the  
314 output guess.  $E_2^*(t)$  is then matched to  $E_2(t)$  by varying  $N$  in an iterative fashion. Using this form,  
315 the algorithm in Appendix B is still valid. We used MATLAB to solve this for all cases. The results  
316 are displayed in Fig. 3.

317

#### 318 **4 Discussion**

319

320 The small aspect ratio of the WU-PAM limits wall interactions, preventing laminar flow  
321 development due to absence of a boundary layer. This suggests the flow field would then depend  
322 on inlet/outlet geometries or volumetric flowrate. Though, for a fixed spacetime of 78s, we  
323 observed that different configurations had no significant effect on the RTD (Figs. 3b, d, e). Further,  
324 for configuration I, different spacetimes also had no significant effect. The only case with a marked  
325 change in the signal was for configuration IV at 411s spacetime (Fig. 3f). We attribute this  
326 difference to the low volumetric flowrate, implying that advective transport begins to be less  
327 dominant than turbulent or molecular diffusivity as mode of transport. Such a low spacetime, while  
328 increasing the degree of plug flow, would result in a potentially significant loss of semivolatile or  
329 low volatility gases. Additionally, other modes of transport such as convective effects (vertical  
330 mixing for non-isothermal conditions) could become more apparent, as revealed by Huang et al.  
331 for the Caltech photooxidation flow tube (CPOT) reactor. As mentioned earlier, a detailed



332 phenomenological modeling study of RTDs in the WU-PAM is beyond the scope of this study,  
333 however at more conventional spacetimes, it would be helpful to visualize hydrodynamics to  
334 assess what contacting patterns and state of mixing the reactor exhibits. We thus chose a simple  
335 scenario as a base case for simulation: configuration I at 78s spacetime.

336

337 CFD reveals that the hydrodynamics inside the PAM are far from that of a well-mixed reactor (Fig.  
338 4). This is insightful because the F-Curve of the simulation matches reasonably well with that of  
339 the experiment (Fig. 5) and alone would imply CSTR-like mixing. This is the caveat associated  
340 with interpreting RTDs, and further supports investigation in phenomenological modeling.  
341 Snapshots of the simulation displayed in Fig. 4a-c show there is jetting (short-circuiting),  
342 recirculation, and dead zones. Jetting leads to fluid elements that have a very short residence time  
343 and cause high values of  $E(t)$  at  $t > 0s$ . Recirculation leads to fluid elements spending more time  
344 in the reactor, yielding middle values of  $E(t)$  as elements exit at  $t \sim \bar{t}$ . Stagnation (dead zones) at  
345 the inlet of the reactor cause fluid elements to remain entrained in the reactor for a long time before  
346 exiting the reactor at  $\sim 2-3$  times  $\bar{t}$  at low values of  $E(t)$ , leading to a long tail in the E-Curve. These  
347 three effects together lead to an E-Curve that looks similar to that of a CSTR, but mixing in CSTRs  
348 is dominated by recirculation; meaning that the local concentration of tracer at the exit is identical  
349 to all other locations in the reactor (Zwietering, 1959). Therefore, while tracer tests give a general  
350 idea about contacting patterns, CFD visualizes the hydrodynamics, and help model the reactor.  
351 Plotting the WU-PAM OFR's E-Curves for this scenario on a semilog plot does not yield different  
352 gradients, which would otherwise indicate different volumes for the compartmental modeling of  
353 the jetting, recirculation, and dead volumes (Levenspiel, 2002). The limitation to that statement is  
354 that the E-Curves in this work have been obtained by fitting a one-parameter model, consequences





355 of which should be the focus of future work in conjunction with phenomenological modeling.  
356 Furthermore, our simulations are limited to isothermal conditions, therefore cannot predict  
357 buoyancy effects that could explain spread in the RTD at low flowrates (or low Reynolds numbers)  
358 (Fig. 3f), as observed by Huang et al. (2016).  
359  
360 Lambe et al. (2011a) modeled the Pennsylvania State University PAM (PSU-PAM) reactor using  
361 a compartmental model consisting of two parallel tubular reactors that exhibit Taylor dispersion  
362 (Taylor, 1953), suggesting that their reactor (whose geometry is identical to that of the WU-PAM  
363 OFR) has two main volumes: an active reactor volume, and another volume with entrainment. The  
364 model output matches their experimental data reasonably well, but, they did not decouple the  
365 reactor's E-Curve from that of the setup, implying the match may include phenomena occurring  
366 in other pipes of the setup. Lambe et al. describe RTDs for the two volumes using the axial  
367 dispersion model (ADM) (Taylor, 1953, 1954a, 1954b), which is based on modeling plug or  
368 laminar flow with axial dispersion of material. Generally, as also stated by Huang et al. (2016),  
369 the ADM is valid for regions where the radial Péclet number ( $Pé_r$ ) is less than  $\sim 4$  times the aspect  
370 ratio (length of reactor divided by its cross sectional area), or if  $Pé_r$  is greater than  $\sqrt{48}$  (Aris, 1956;  
371 Taylor, 1954b). Both the PSU-PAM OFR and the WU-PAM OFR meet these requirements under  
372 typical flowrates (see SI, Sect. S4). If the reactor could be described by the ADM, CFD would  
373 show that the entrance and exit effects would be separate from the main flow in the tube – which  
374 is not the case for the simplified geometry of configuration I. We do not know how well they apply  
375 to the other configurations. At no point inside the reactor does pipe flow fully develop, so the high  
376 aspect ratio concept (Kang et al., 2007) does not allow a velocity profile to become established  
377 with the current end caps used. Thus, although  $Pé_r$  appears acceptable, the inlet and outlet regions



378 should be re-engineered to allow formation of fully developed pipe flow in the main cylinder for  
379 the ADM to be valid. While the E-Curve for configuration II is similar to that of configuration I at  
380 78s spacetime, it would be helpful to run CFD on that configuration at different spacetimes to  
381 observe if, and if so at what spacetime, the sparger and baffles efficiently suppress jetting.  
382 Unfortunately, our CFD mesh could not be refined enough to capture the geometry of those without  
383 sacrificing valuable computational time.

384

385 Instead, we chose to apply the use of an inlet cone ( $45^\circ$  angle, 4.94'' length) and outlet peripherals  
386 to simulate a more attenuated inlet and exit from sudden aperture. The results are displayed in Fig.  
387 6. While the size of the jet appears to be broader compared to simulations in Fig. 5 (unaltered  
388 PAM geometry), it is nonetheless present. Furthermore, recirculation in the form of backmixing is  
389 evident towards the front, and stagnation close to the walls and corners persists. From the velocity  
390 field (Fig. 6 center figure), a smaller cone angle that follows the contour of the light blue velocity  
391 field could prevent backmixing.

392

### 393 **5 Potential implications**

394

395 Recent modeling work assumes plug flow behavior in OFRs (Li et al., 2015; Peng et al., 2015,  
396 2016). Li et al. state that correcting for the non-ideal E-Curve in their OFR would account for  
397 ~10% error in their results, which is less than the overall model uncertainty. However, for  
398 compounds with low  $\text{OHR}_{\text{ext}}$ , contacting could influence the model results to a greater extent. By  
399 taking a ratio of characteristic reaction time (e.g.,  $\text{OHR}_{\text{ext}}$ ) to the characteristic transport time, one  
400 can define the Damköhler number ( $\text{Da}_n$ ). Considering spacetimes of 52-411s (as per this study),



401 the value of  $Da_n$  can be between 5200 and 41100 for a compound with  $OHR_{ext} \sim 100s^{-1}$ . Since  
402 reaction timescales are  $10^4$  times faster than transport timescales, contact patterns won't matter to  
403 a large degree. However, the value of  $Da_n$  can be between 5.2 and 41.1 for a compound with  
404  $OHR_{ext} \sim 0.1s^{-1}$ , in which case contacting patterns may play a more significant role. This could be  
405 the case for heterogenous reactions, diffusion-limited reactions, or semivolatile compound  
406 (SVOC) oxidation that exhibit slow gas-particle partitioning. Furthermore, combining  
407 phenomenological model to an associated RTD can impact kinetics (and yields) further. The RTD  
408 generated by Lambe et al. (2011) employed in Li et al. (2015) may lead to greater than 10% error  
409 if the 2 PFRs in parallel model suggested by Lambe et al. (2011) is not applicable. In these  
410 scenarios, ensuring a high degree of plug flow can not only maximize exposure, but minimize the  
411 distribution of aged compounds (e.g., first or second generation compounds) that are due to  
412 different exit ages because of recirculation or stagnation. This configuration would suit a  
413 laboratory experiment with slow kinetics, where concentrations can be made high enough to where  
414 wall losses aren't an issue. However, this configuration may not suit a field deployment where  
415 trace compounds have high  $OHR_{ext}$  and can be easily lost to reactor walls, in which case ensuring  
416 a high degree of mixing would be beneficial.

417

## 418 **6 Conclusion**

419

420 The WU-PAM reactor's hydrodynamics are complex, and even though the E-Curve looks simple,  
421 applying a compartmental model (phenomenological modeling) to obtain an analytical E-Curve  
422 (rather than the empirically-based TIS E-Curve) can be challenging. Having too sudden an aperture  
423 at the entrance zone leads to dead volumes at the inlet corners. We cannot confirm if the sparger



424 design helps reduce dead volume, but tracer tests suggest it doesn't appear to affect the degree of  
425 plug flow under standard operating spacetimes (52-156s). The reactor is described neither by back  
426 mixing, plug flow, nor by the ADM in any configuration. However, for configuration IV at 411s  
427 spacetime, a noticeable shift towards plug flow behavior is observed, perhaps due to a combined  
428 effect of internals and low inlet velocity. We note that the E-Curves we obtain are not as accurate  
429 as an E-Curve numerically obtained by direct deconvolution, since we are forcing a closed form  
430 solution on our data. We further note the need for phenomenological modeling.

431

432 Tapered ends on the inlet and the outlet would help to develop a steady flow profile at the inlet  
433 and avoid recirculation at the outlet, however the cone angle should be predetermined by CFD if  
434 possible. By improving simulations to include temperature gradients induced when the internal  
435 lamps are on, and refining the mesh to capture internals, the ADM should be revisited as a model  
436 to describe the PAM reactor. If the ADM satisfactorily describes the PAM reactor's RTD, kinetics  
437 should be easier to obtain, and diffusivity values using the Aris-Taylor relationship (Aris, 1956)  
438 can even be obtained. This could help assess whether processes are reaction limited or diffusion  
439 limited, arguing the reactor validity in experimental setups. At that point, the reactors would be  
440 regulated by only one parameter, their flowrate. This parameter would be adjusted to achieve  
441 desired spacetimes depending on  $OHR_{ext}$ . Finally, to obtain accurate experimental RTDs,  
442 achieving a functional direct deconvolution code should be focus of future development. The  
443 implementation of this technique can be extended to drift tubes in mass spectrometers, as those are  
444 essentially flow tube reactors where ionization efficiency can be strongly influenced by mixing.

445

446 **Acknowledgements**



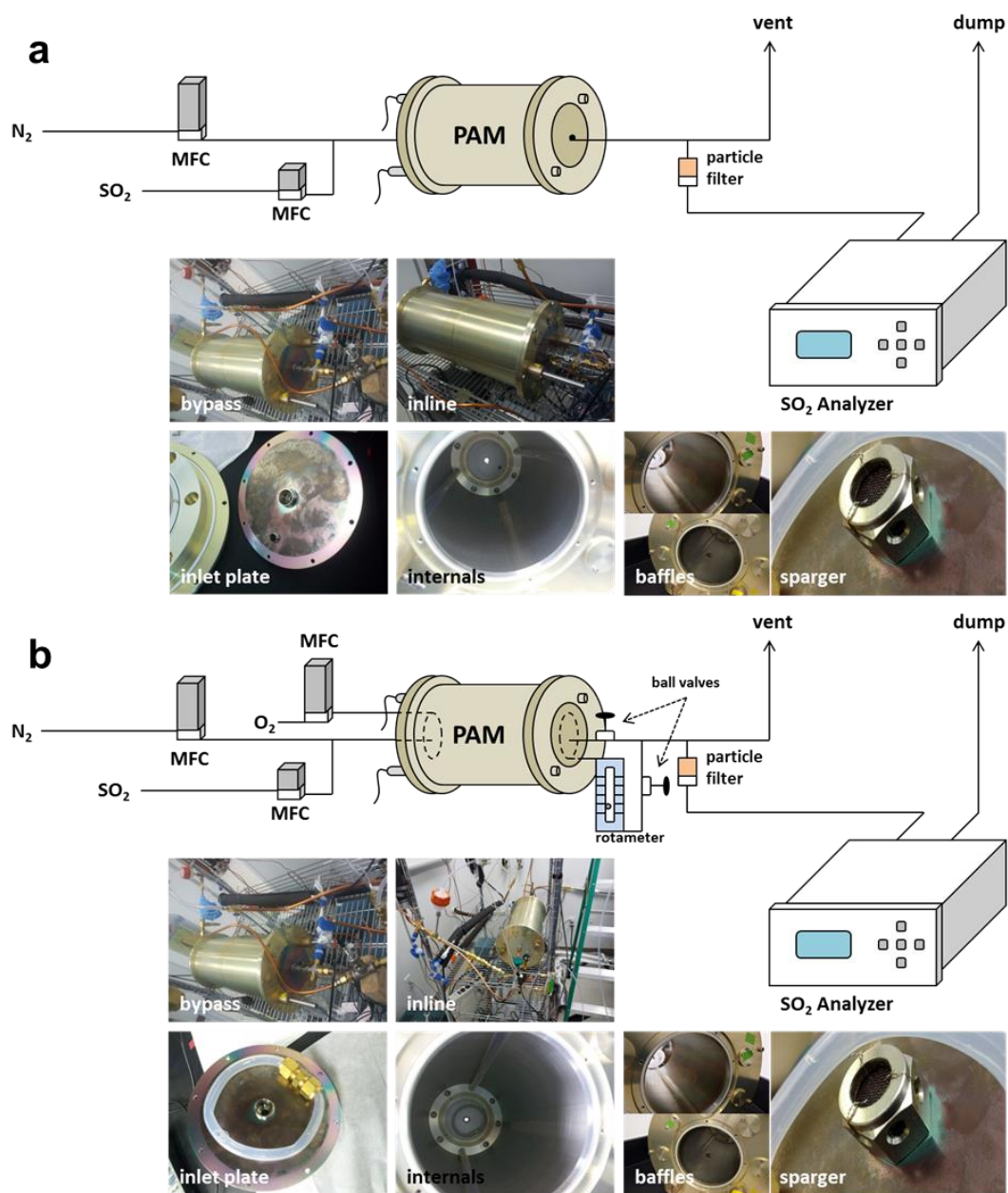
447

448 We would like to express appreciation for the valuable discussions with Prof. Jay Turner, Prof.  
449 James Ballard, Christopher Oxford, David Hagan, and Tim Lee at Washington University in St.  
450 Louis, and valuable correspondence with Prof. William Brune at the Pennsylvania State University  
451 and Dr. Andrew Lambe at Aerodyne Research Inc. We would also like to thank ENGYS and Prof.  
452 Milorad Duduković's CREL resources, who provided the necessary computational power to run  
453 CFD. This work was partly funded by the National Science Foundation (NSF) CBET Award  
454 #1236865, and NSF CBET Award #1437933.

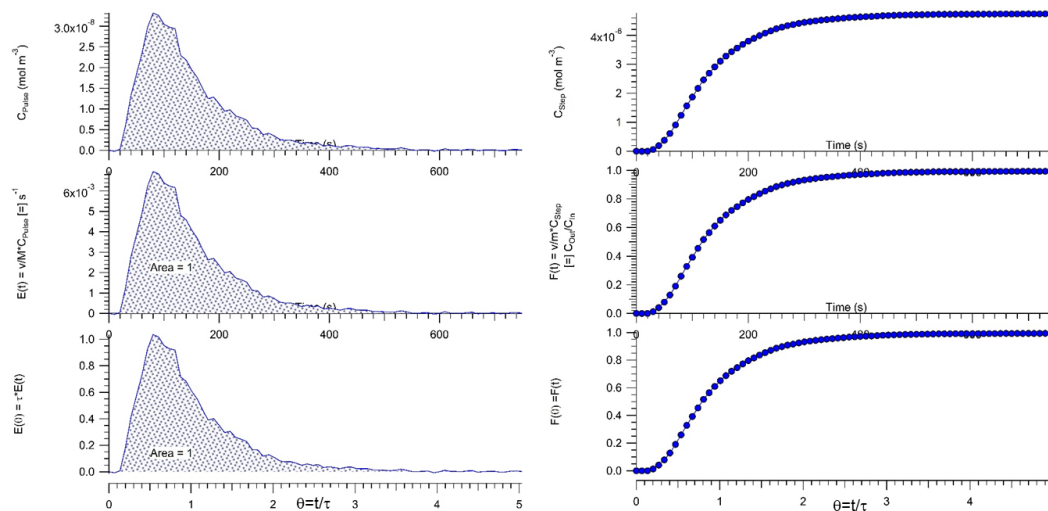
455

456 **Figures**

457



458  
 459 Figure 1: Experimental setup for tracer studies for a) one inlet and one outlet and b) peripheral  
 460 inlets and outlets. The main difference is the presence of the ring sparger in b).  
 461



462

463

Figure 2: Tracer tests at  $10 \text{ L min}^{-1}$  (78s spacetime) through the reactor for configuration I. This figure serves as an illustrative example for non-dimensionalizing tracer response curves.

464

465

466

467

468

469

470

471

472

473

474

475

476

477

478

479

480

481

482

483

484

485

486

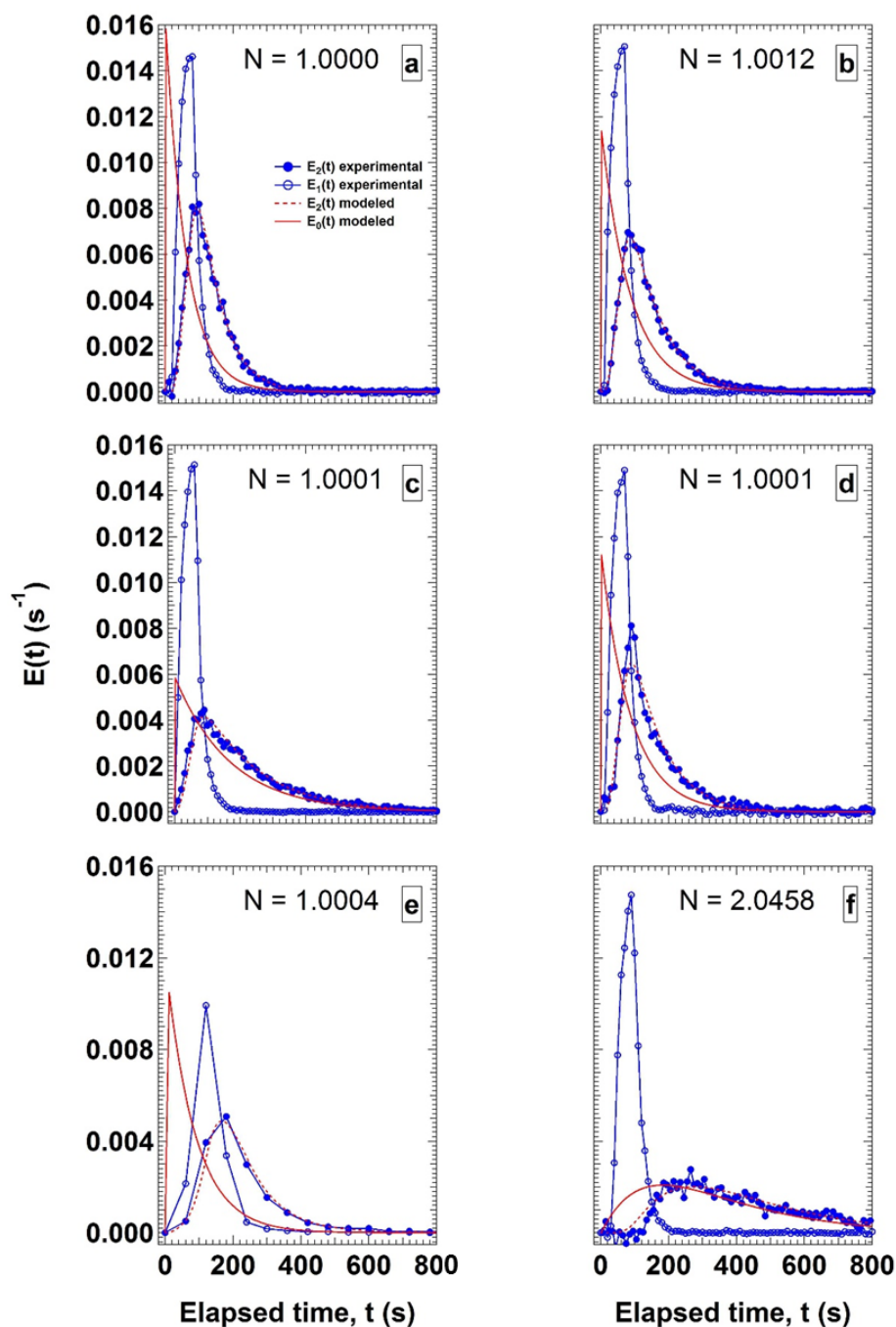
487

488

489

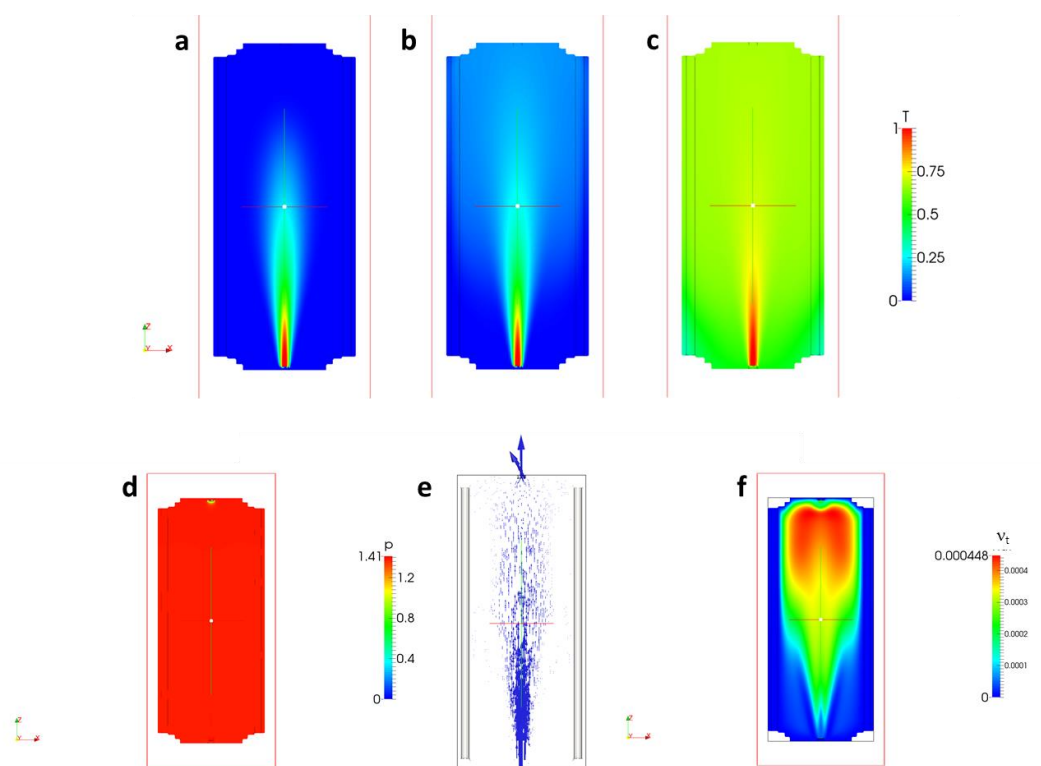
490

491

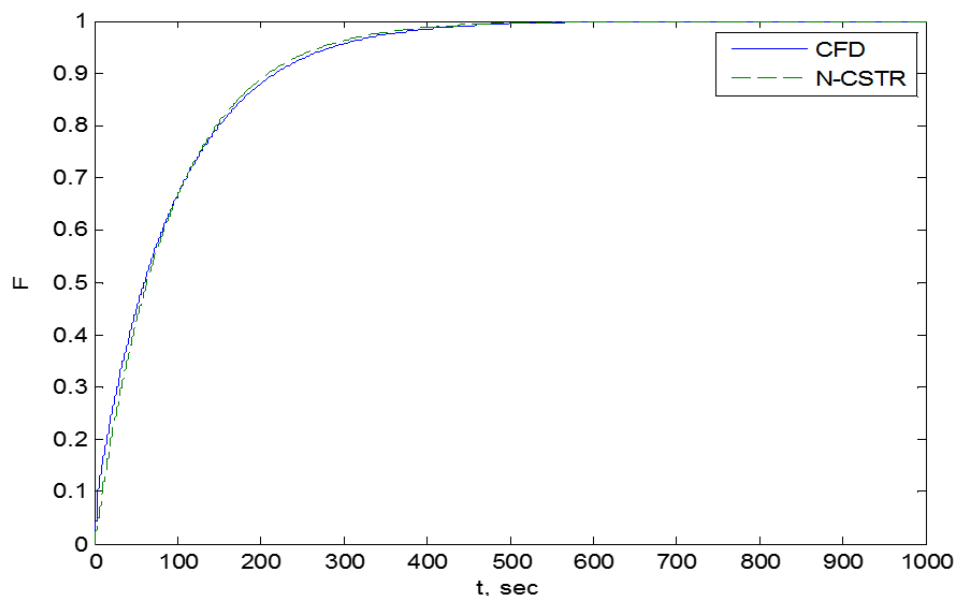


492  
 493 Figure 3: E-Curves for the WU-PAM configuration I at a) 52s b) 78s c) 156s spacetimes, at 78s  
 494 spacetimes for d) configuration II e) configuration III, and f) for configuration IV at 411s  
 495 spacetime. Details on the configurations are in the Methods section.

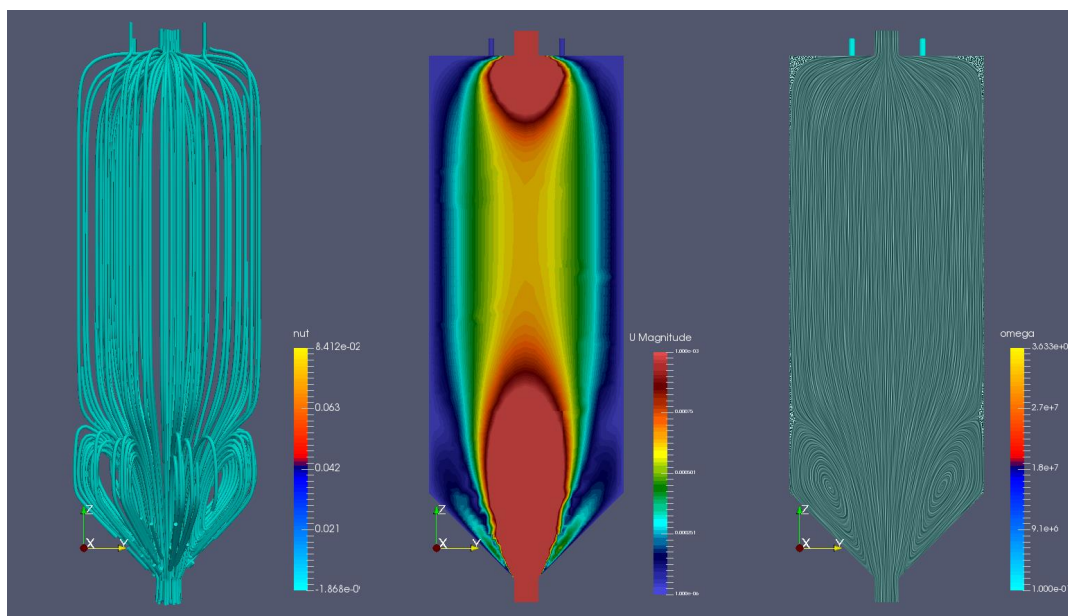




496  
497 Figure 4: CFD output for configuration I at 78s spacetime: snapshots at a) 1s b) 10s and c) 100s of  
498 runtime, and d) pressure field, e) velocity field, and f) turbulent diffusivity field. Color scales are  
499 dimensionless scalar concentration for the tracer (a-c), Bar for the pressure field (d), and cSt for  
500 the kinematic viscosity (f).  
501  
502  
503  
504  
505  
506  
507  
508  
509  
510  
511  
512  
513  
514  
515



516 Figure 5: Comparison of F-Curve output between CFD and tracer test for configuration I at 78s  
517 spacetime.  
518



519 Figure 6: CFD analysis on the effect of inlet cone and peripheral outlets on fluid flow. All figures  
520 represent a visualization of the flow field, with color scales representing (from left to right):  
521 kinematic viscosity, velocity, and  $\omega$ . The 3D representation on the leftmost figure highlights the  
522 uniformity of the recirculation region.  
523



524 **Appendix A: The use of E-Curves and F-Curves**

525

526 To determine RTDs, we injected tracer in a steady stream rather than a single pulse. This prolonged  
527 and constant injection, which we call a step input, gave us  $F(t)$ , from which we can derive  $E(t)$  as  
528 follows:

$$F(t) = \frac{v}{m} C_{step} \quad (A1)$$

$$E(t) = \frac{dF(t)}{dt}, \quad (A2)$$

529 where  $v$  is the volumetric flowrate in  $\text{m}^3\text{s}^{-1}$ ,  $m$  is the molar flowrate of the tracer in  $\text{mol s}^{-1}$ , and  
530  $C_{step}$  is the concentration of the tracer for a step input in  $\text{mol m}^{-3}$ . Therefore,  $F(t)$  is dimensionless,  
531 and  $E(t)$  in this example has units of  $\text{s}^{-1}$ . The area under the E-Curve is unity, representing the PDF  
532 of the system:

$$\int_0^{\infty} E(t) dt = 1. \quad (A3)$$

533 Similarly, for the dimensionless domain

$$\int_0^{\infty} E(\theta) d\theta = 1. \quad (A4)$$

534 And if we take  $\bar{t}$  to be the mean residence time of the reactor, then

$$\theta = \frac{t}{\bar{t}}. \quad (A5)$$

535 The additional utility of the dimensionless domain is that for reactors of different sizes, built to  
536 behave the same, the RTD is numerically identical. For example, if PAM OFRs are operated in  
537 different ways (e.g., they operate at different flowrates) or are built in different sizes but display  
538 the same E-Curve in the dimensionless domain, then their performance will be identical, and their  
539 mean residence time will always occur at  $\theta = 1$ . This identity would apply for the F-Curve as well  
540 in both domains, where from Eq. (A2) we can see that



541

$$F(t) = \int_0^t E(t) dt \quad (\text{A6})$$

$$F(\theta) = \int_0^t E(\theta) d\theta. \quad (\text{A7})$$

542 The mathematical properties of interest for PDFs are their moments: These have quantitative  
 543 meanings in E-Curve analysis. A general equation for the moments of a function  $f(x)$  is

$$\mu_n = \int_{-\infty}^{\infty} x^n \cdot f(x) dx, \quad (\text{A8})$$

544 where  $\mu_n$  is the  $n$ th moment of the distribution. If we consider a raw  $C(t)$  dataset from our tracer,  
 545 we can derive the moments:

$$\frac{\int_0^{\infty} C(t) dt}{\int_0^{\infty} C(t) dt} = \int_0^{\infty} E(t) dt = 1 = \mu_0 \quad (\text{A9})$$

$$\frac{\int_0^{\infty} t \cdot C(t) dt}{\int_0^{\infty} C(t) dt} = \int_0^{\infty} t \cdot E(t) dt = \bar{t} = \mu_1. \quad (\text{A10})$$

546 Here, we are interested in the first moment, which represents the mean residence time. For higher  
 547 moments, we use the central moments of the distribution since we are interested in quantities like  
 548 variance, skewness, and kurtosis around the mean (and not around zero). This alters Eq. (A8) as  
 549 follows:

$$\mu_n = \int_{-\infty}^{\infty} (x - a)^n \cdot f(x) dx; n \geq 2, \quad (\text{A11})$$

550 where  $a$  is a constant, and is generally the mean of the distribution ( $\bar{t}$  in this case). Thus, the second  
 551 (central) moment of the E-Curve becomes

$$\frac{\int_0^{\infty} (t - \bar{t})^2 \cdot C(t) dt}{\int_0^{\infty} C(t) dt} = \int_0^{\infty} (t - \bar{t})^2 \cdot E(t) dt = \sigma^2 = \quad (\text{A12})$$

$\mu_2$ ,



552 where  $\sigma^2$  has a clear physical meaning, and is the variance around the mean. Higher moments  
 553 (skewness and kurtosis) can be of use, and require additional math, but are not addressed in this  
 554 work.

555

### 556 **Appendix B: Algorithm for direct deconvolution**

557

558 Here, we perform an inverse operation to Eq. (7) (Sun, 2010) and work towards an output curve:

$$E_2(t) = \int_0^t E_1(t-t') \cdot E_0(t') dt'. \quad (\text{B1})$$

559 In discrete form, taking a constant time step  $\Delta t$ , we can take a datapoint at  $t_i = i\Delta t$ ,

$$E_{2N}(t_i) = \sum_{i=1}^N \int_{t_{i-1}}^{t_i} E_1(t_N - t') \cdot E_0(t') dt'. \quad (\text{B2})$$

560 If we then assume that the functions  $E_1(t-t')$  and  $E_0(t')$  are constant for the interval  $t_{i-1} \leq t' \leq$

561  $t_i$ , we can simplify the integral:

$$E_1(t_N - t') = \frac{1}{2} (E_1|_{N-1} + E_1|_{N-i+1}) \quad (\text{B3})$$

$$E_0(t') = \frac{1}{2} (E_0|_i + E_0|_{i-1}) \quad (\text{B4})$$

$$\int_{t_{i-1}}^{t_i} E_1(t_N - t') \cdot E_0(t') dt' = \frac{1}{4} (E_1|_{N-1} + E_1|_{N-i+1}) (E_0|_i + E_0|_{i-1}) \Delta t. \quad (\text{B5})$$

562 Now, Eq. (B2) becomes

$$E_{2N}(t_i) = \sum_{i=1}^N \frac{1}{4} (E_1|_{N-1} + E_1|_{N-i+1}) (E_0|_i + E_0|_{i-1}) \Delta t. \quad (\text{B6})$$



563 From experimental data, we can accurately collect datapoints for  $(E_1|_{N-1} + E_1|_{N-i+1})$  as well as  
 564  $E_2(t_i)$ , so we need to rearrange for  $(E_0|_i + E_0|_{i-1})$ , which has to be solved numerically in matrix  
 565 form. Let

$$\alpha_i = \beta_i = \frac{1}{4}(E_1|_{N-1} + E_1|_{N-i+1}) \quad (\text{B7})$$

$$A_{N,i} = \begin{cases} \alpha_i + \beta_{i+1} & i = 1, 2, \dots, (N-1) \\ \alpha_N & i = N \end{cases}. \quad (\text{B8})$$

566 Upon the initial condition

$$B_N = \frac{E_2(t_N)}{\Delta t} - \beta_1 E_0|_0, \quad (\text{B9})$$

567 we have that

$$B_N = \sum_{i=1}^N A_{N,i} E_0|_i. \quad (\text{B10})$$

568 Finally,

$$\overrightarrow{E_0(t)} = \overrightarrow{A}^{-1} \overrightarrow{B}. \quad (\text{B11})$$

569

## 570 References

571

572 Aris, R.: On the Dispersion of a Solute in a Fluid Flowing through a Tube, Proc. R. Soc. Math.  
 573 Phys. Eng. Sci., 235(1200), 67–77, doi:10.1098/rspa.1956.0065, 1956.

574 Bourne, J. R.: Mixing and the Selectivity of Chemical Reactions, Org. Process Res. Dev., 7(4),  
 575 471–508, doi:10.1021/op020074q, 2003.

576 Brune, W. H., Schwab, J. J. and Anderson, J. G.: Laser magnetic resonance, resonance  
 577 fluorescence, resonance absorption studies of the reaction kinetics of  $O + OH \rightarrow H + O_2$ ,  $O + HO_2$   
 578  $\rightarrow OH + O_2$ ,  $N + OH \rightarrow H + NO$ ,  $N + HO_2 \rightarrow$  products at 300 K between 1 and 5 torr, J. Phys.  
 579 Chem., 87(22), 4503–4514, doi:10.1021/j100245a034, 1983.

580 Bruns, E. A., El Haddad, I., Keller, A., Klein, F., Kumar, N. K., Pieber, S. M., Corbin, J. C.,  
 581 Slowik, J. G., Brune, W. H., Baltensperger, U. and Prévôt, A. S. H.: Inter-comparison of laboratory  
 582 smog chamber and flow reactor systems on organic aerosol yield and composition, Atmospheric  
 583 Meas. Tech., 8(6), 2315–2332, doi:10.5194/amt-8-2315-2015, 2015.



- 584 Canagaratna, M. R., Jayne, J. T., Jimenez, J. L., Allan, J. D., Alfarra, M. R., Zhang, Q., Onasch,  
585 T. B., Drewnick, F., Coe, H., Middlebrook, A., Delia, A., Williams, L. R., Trimborn, A. M.,  
586 Northway, M. J., DeCarlo, P. F., Kolb, C. E., Davidovits, P. and Worsnop, D. R.: Chemical and  
587 microphysical characterization of ambient aerosols with the aerodyne aerosol mass spectrometer,  
588 *Mass Spectrom. Rev.*, 26(2), 185–222, doi:10.1002/mas.20115, 2007.
- 589 Cazorla, M. and Brune, W. H.: Measurement of Ozone Production Sensor, *Atmospheric Meas.*  
590 *Tech.*, 3(3), 545–555, doi:10.5194/amt-3-545-2010, 2010.
- 591 Chhabra, P. S., Lambe, A. T., Canagaratna, M. R., Stark, H., Jayne, J. T., Onasch, T. B.,  
592 Davidovits, P., Kimmel, J. R. and Worsnop, D. R.: Application of high-resolution time-of-flight  
593 chemical ionization mass spectrometry measurements to estimate volatility distributions of  $\alpha$ -  
594 pinene and naphthalene oxidation products, *Atmospheric Meas. Tech.*, 8(1), 1–18,  
595 doi:10.5194/amt-8-1-2015, 2015.
- 596 Claeys, M.: Formation of Secondary Organic Aerosols Through Photooxidation of Isoprene,  
597 *Science*, 303(5661), 1173–1176, doi:10.1126/science.1092805, 2004.
- 598 Crounse, J. D., McKinney, K. A., Kwan, A. J. and Wennberg, P. O.: Measurement of Gas-Phase  
599 Hydroperoxides by Chemical Ionization Mass Spectrometry, *Anal. Chem.*, 78(19), 6726–6732,  
600 doi:10.1021/ac0604235, 2006.
- 601 Crump, J. G. and Seinfeld, J. H.: Aerosol behavior in the continuous stirred tank reactor, *AIChE*  
602 *J.*, 26(4), 610–616, doi:10.1002/aic.690260412, 1980.
- 603 Crump, J. G., Flagan, R. C. and Seinfeld, J. H.: Particle Wall Loss Rates in Vessels, *Aerosol Sci.*  
604 *Technol.*, 2(3), 303–309, doi:10.1080/02786828308958636, 1982.
- 605 Danckwerts, P. V.: Continuous flow systems, *Chem. Eng. Sci.*, 2(1), 1–13, doi:10.1016/0009-  
606 2509(53)80001-1, 1953.
- 607 Deckwer, W.-D.: Non-isobaric bubble columns with variable gas velocity, *Chem. Eng. Sci.*, 31(4),  
608 309–317, doi:10.1016/0009-2509(76)85076-2, 1976.
- 609 Ezell, M. J., Johnson, S. N., Yu, Y., Perraud, V., Bruns, E. A., Alexander, M. L., Zelenyuk, A.,  
610 Dabdub, D. and Finlayson-Pitts, B. J.: A New Aerosol Flow System for Photochemical and  
611 Thermal Studies of Tropospheric Aerosols, *Aerosol Sci. Technol.*, 44(5), 329–338,  
612 doi:10.1080/02786821003639700, 2010.
- 613 Fogler, H. S.: Elements of chemical reaction engineering, 4th ed., Prentice Hall PTR, Upper Saddle  
614 River, NJ., 2006.
- 615 George, I. J. and Abbatt, J. P. D.: Chemical evolution of secondary organic aerosol from OH-  
616 initiated heterogeneous oxidation, *Atmospheric Chem. Phys.*, 10(12), 5551–5563,  
617 doi:10.5194/acp-10-5551-2010, 2010.
- 618 George, I. J., Vlasenko, A., Slowik, J. G., Broekhuizen, K. and Abbatt, J. P. D.: Heterogeneous  
619 oxidation of saturated organic aerosols by hydroxyl radicals: uptake kinetics, condensed-phase



- 620 products, and particle size change, *Atmospheric Chem. Phys.*, 7(16), 4187–4201, doi:10.5194/acp-  
621 7-4187-2007, 2007.
- 622 de Gouw, J. and Warneke, C.: Measurements of volatile organic compounds in the earth's  
623 atmosphere using proton-transfer-reaction mass spectrometry, *Mass Spectrom. Rev.*, 26(2), 223–  
624 257, doi:10.1002/mas.20119, 2007.
- 625 Haagen-Smit, A. J.: Chemistry and Physiology of Los Angeles Smog, *Ind. Eng. Chem.*, 44(6),  
626 1342–1346, doi:10.1021/ie50510a045, 1952.
- 627 Haagen-Smit, A. J.: Photochemistry and Smog, *J. Air Pollut. Control Assoc.*, 13(9), 444–454,  
628 doi:10.1080/00022470.1963.10468205, 1963.
- 629 Haagen-Smit, A. J.: A Lesson from the Smog Capital of the World, *Proc. Natl. Acad. Sci.*, 67(2),  
630 887–897, doi:10.1073/pnas.67.2.887, 1970.
- 631 Hamed, M.: Hydrodynamics, Mixing, and Mass Transfer in Bubble Columns with Internals, PhD,  
632 Washington University in St. Louis, Saint Louis., 2012.
- 633 Han, L.: Hydrodynamics, back-mixing, and mass transfer in a slurry bubble column reactor for  
634 Fischer-Tropsch alternative fuels, DSc, Washington University in St. Louis, Saint Louis., 2007.
- 635 Hansel, A., Jordan, A., Holzinger, R., Prazeller, P., Vogel, W. and Lindinger, W.: Proton transfer  
636 reaction mass spectrometry: on-line trace gas analysis at the ppb level, *Int. J. Mass Spectrom. Ion  
637 Process.*, 149–150, 609–619, doi:10.1016/0168-1176(95)04294-U, 1995.
- 638 Howard, C. J.: Kinetic measurements using flow tubes, *J. Phys. Chem.*, 83(1), 3–9,  
639 doi:10.1021/j100464a001, 1979.
- 640 Huang, Y., Coggon, M. M., Zhao, R., Lignell, H., Bauer, M. U., Flagan, R. C. and Seinfeld, J. H.:  
641 The Caltech Photooxidation Flow Tube Reactor &ndash; I: Design and Fluid Dynamics,  
642 *Atmospheric Meas. Tech. Discuss.*, 1–36, doi:10.5194/amt-2016-282, 2016.
- 643 Jayne, J. T., Leard, D. C., Zhang, X., Davidovits, P., Smith, K. A., Kolb, C. E. and Worsnop, D.  
644 R.: Development of an Aerosol Mass Spectrometer for Size and Composition Analysis of  
645 Submicron Particles, *Aerosol Sci. Technol.*, 33(1–2), 49–70, doi:10.1080/027868200410840,  
646 2000.
- 647 Kamens, R. M., Gery, M. W., Jeffries, H. E., Jackson, M. and Cole, E. I.: Ozone-isoprene  
648 reactions: Product formation and aerosol potential, *Int. J. Chem. Kinet.*, 14(9), 955–975,  
649 doi:10.1002/kin.550140902, 1982.
- 650 Kang, E., Root, M. J., Toohey, D. W. and Brune, W. H.: Introducing the concept of Potential  
651 Aerosol Mass (PAM), *Atmospheric Chem. Phys.*, 7(22), 5727–5744, doi:10.5194/acp-7-5727-  
652 2007, 2007.





- 653 Kang, E., Toohey, D. W. and Brune, W. H.: Dependence of SOA oxidation on organic aerosol  
654 mass concentration and OH exposure: experimental PAM chamber studies, *Atmospheric Chem.*  
655 *Phys.*, 11(4), 1837–1852, doi:10.5194/acp-11-1837-2011, 2011.
- 656 Katrib, Y., Biskos, G., Buseck, P. R., Davidovits, P., Jayne, J. T., Mochida, M., Wise, M. E.,  
657 Worsnop, D. R. and Martin, S. T.: Ozonolysis of Mixed Oleic-Acid/Stearic-Acid Particles:  
658 Reaction Kinetics and Chemical Morphology, *J. Phys. Chem. A*, 109(48), 10910–10919,  
659 doi:10.1021/jp054714d, 2005.
- 660 Keller, A. and Burtscher, H.: A continuous photo-oxidation flow reactor for a defined  
661 measurement of the SOA formation potential of wood burning emissions, *J. Aerosol Sci.*, 49, 9–  
662 20, doi:10.1016/j.jaerosci.2012.02.007, 2012.
- 663 Kessler, S. H., Smith, J. D., Che, D. L., Worsnop, D. R., Wilson, K. R. and Kroll, J. H.: Chemical  
664 Sinks of Organic Aerosol: Kinetics and Products of the Heterogeneous Oxidation of Erythritol and  
665 Levoglucosan, *Environ. Sci. Technol.*, 44(18), 7005–7010, doi:10.1021/es101465m, 2010.
- 666 Kessler, S. H., Nah, T., Daumit, K. E., Smith, J. D., Leone, S. R., Kolb, C. E., Worsnop, D. R.,  
667 Wilson, K. R. and Kroll, J. H.: OH-Initiated Heterogeneous Aging of Highly Oxidized Organic  
668 Aerosol, *J. Phys. Chem. A*, 116(24), 6358–6365, doi:10.1021/jp212131m, 2012.
- 669 Keyser, L. F.: Absolute rate constant of the reaction  $\text{OH} + \text{H}_2\text{O}_2 \rightarrow \text{HO}_2 + \text{H}_2\text{O}$  from 245 to 423  
670 K, *J. Phys. Chem.*, 84(13), 1659–1663, doi:10.1021/j100450a001, 1980.
- 671 Keyser, L. F.: High-pressure flow kinetics. A study of the hydroxyl + hydrogen chloride reaction  
672 from 2 to 100 torr, *J. Phys. Chem.*, 88(20), 4750–4758, doi:10.1021/j150664a061, 1984.
- 673 Knopf, D. A., Anthony, L. M. and Bertram, A. K.: Reactive Uptake of  $\text{O}_3$  by Multicomponent and  
674 Multiphase Mixtures Containing Oleic Acid, *J. Phys. Chem. A*, 109(25), 5579–5589,  
675 doi:10.1021/jp0512513, 2005.
- 676 Kroll, J. H. and Seinfeld, J. H.: Chemistry of secondary organic aerosol: Formation and evolution  
677 of low-volatility organics in the atmosphere, *Atmos. Environ.*, 42(16), 3593–3624,  
678 doi:10.1016/j.atmosenv.2008.01.003, 2008.
- 679 Kroll, J. H., Ng, N. L., Murphy, S. M., Flagan, R. C. and Seinfeld, J. H.: Secondary Organic  
680 Aerosol Formation from Isoprene Photooxidation, *Environ. Sci. Technol.*, 40(6), 1869–1877,  
681 doi:10.1021/es0524301, 2006.
- 682 Kroll, J. H., Smith, J. D., Worsnop, D. R. and Wilson, K. R.: Characterisation of lightly oxidised  
683 organic aerosol formed from the photochemical aging of diesel exhaust particles, *Environ. Chem.*,  
684 9(3), 211, doi:10.1071/EN11162, 2012.
- 685 Lamb, J. J., Molina, L. T., Smith, C. A. and Molina, M. J.: Rate constant of the hydroxy radical +  
686 hydrogen peroxide  $\cdot\text{fwdarw}$  hydroperoxo radical + water reaction, *J. Phys. Chem.*, 87(22), 4467–  
687 4470, doi:10.1021/j100245a028, 1983.



- 688 Lambe, A. T., Ahern, A. T., Williams, L. R., Slowik, J. G., Wong, J. P. S., Abbatt, J. P. D., Brune,  
689 W. H., Ng, N. L., Wright, J. P., Croasdale, D. R., Worsnop, D. R., Davidovits, P. and Onasch, T.  
690 B.: Characterization of aerosol photooxidation flow reactors: heterogeneous oxidation, secondary  
691 organic aerosol formation and cloud condensation nuclei activity measurements, *Atmospheric*  
692 *Meas. Tech.*, 4(3), 445–461, doi:10.5194/amt-4-445-2011, 2011a.
- 693 Lambe, A. T., Onasch, T. B., Massoli, P., Croasdale, D. R., Wright, J. P., Ahern, A. T., Williams,  
694 L. R., Worsnop, D. R., Brune, W. H. and Davidovits, P.: Laboratory studies of the chemical  
695 composition and cloud condensation nuclei (CCN) activity of secondary organic aerosol (SOA)  
696 and oxidized primary organic aerosol (OPOA), *Atmospheric Chem. Phys. Discuss.*, 11(5), 13617–  
697 13653, doi:10.5194/acpd-11-13617-2011, 2011b.
- 698 Lambe, A. T., Onasch, T. B., Croasdale, D. R., Wright, J. P., Martin, A. T., Franklin, J. P., Massoli,  
699 P., Kroll, J. H., Canagaratna, M. R., Brune, W. H., Worsnop, D. R. and Davidovits, P.: Transitions  
700 from Functionalization to Fragmentation Reactions of Laboratory Secondary Organic Aerosol  
701 (SOA) Generated from the OH Oxidation of Alkane Precursors, *Environ. Sci. Technol.*, 46(10),  
702 5430–5437, doi:10.1021/es300274t, 2012.
- 703 Lambe, A. T., Cappa, C. D., Massoli, P., Onasch, T. B., Forestieri, S. D., Martin, A. T., Cummings,  
704 M. J., Croasdale, D. R., Brune, W. H., Worsnop, D. R. and Davidovits, P.: Relationship between  
705 Oxidation Level and Optical Properties of Secondary Organic Aerosol, *Environ. Sci. Technol.*,  
706 130606090408002, doi:10.1021/es401043j, 2013.
- 707 Lambe, A. T., Chhabra, P. S., Onasch, T. B., Brune, W. H., Hunter, J. F., Kroll, J. H., Cummings,  
708 M. J., Brogan, J. F., Parmar, Y., Worsnop, D. R., Kolb, C. E. and Davidovits, P.: Effect of oxidant  
709 concentration, exposure time, and seed particles on secondary organic aerosol chemical  
710 composition and yield, *Atmospheric Chem. Phys.*, 15(6), 3063–3075, doi:10.5194/acp-15-3063-  
711 2015, 2015.
- 712 Leone, J. A., Flagan, R. C., Grosjean, D. and Seinfeld, J. H.: An outdoor smog chamber and  
713 modeling study of toluene-NO<sub>x</sub> photooxidation, *Int. J. Chem. Kinet.*, 17(2), 177–216,  
714 doi:10.1002/kin.550170206, 1985.
- 715 Levenspiel, O.: *Chemical reaction engineering*, 3rd ed., Wiley, New York., 1999.
- 716 Levenspiel, O.: *The chemical reactor omnibook*, OSU Book Stores, Corvallis, Or., 2002.
- 717 Li, R., Palm, B. B., Ortega, A. M., Hlywiak, J., Hu, W., Peng, Z., Day, D. A., Knote, C., Brune,  
718 W. H., de Gouw, J. A. and Jimenez, J. L.: Modeling the Radical Chemistry in an Oxidation Flow  
719 Reactor: Radical Formation and Recycling, Sensitivities, and the OH Exposure Estimation  
720 Equation, *J. Phys. Chem. A*, 119(19), 4418–4432, doi:10.1021/jp509534k, 2015.
- 721 Liu, P. F., Abdelmalki, N., Hung, H.-M., Wang, Y., Brune, W. H. and Martin, S. T.: Ultraviolet  
722 and visible complex refractive indices of secondary organic material produced by photooxidation  
723 of the aromatic compounds toluene and m-xylene, *Atmospheric Chem. Phys.*, 15(3), 1435–1446,  
724 doi:10.5194/acp-15-1435-2015, 2015.



- 725 MacMullin, R. B. and Weber Jr., M.: The theory of short-circuiting in continuous-flow mixing  
726 vessels in series and the kinetics of chemical reactions in such systems, *Trans. Am. Inst. Chem.*  
727 *Eng.*, 31, 409–458, 1935.
- 728 Massoli, P., Lambe, A. T., Ahern, A. T., Williams, L. R., Ehn, M., Mikkilä, J., Canagaratna, M.  
729 R., Brune, W. H., Onasch, T. B., Jayne, J. T., Petäjä, T., Kulmala, M., Laaksonen, A., Kolb, C. E.,  
730 Davidovits, P. and Worsnop, D. R.: Relationship between aerosol oxidation level and hygroscopic  
731 properties of laboratory generated secondary organic aerosol (SOA) particles:  
732 HYGROSCOPICITY OF LABORATORY SOA, *Geophys. Res. Lett.*, 37(24), n/a-n/a,  
733 doi:10.1029/2010GL045258, 2010.
- 734 McNeill, V. F., Yatavelli, R. L. N., Thornton, J. A., Stipe, C. B. and Landgrebe, O.: Heterogeneous  
735 OH oxidation of palmitic acid in single component and internally mixed aerosol particles:  
736 vaporization and the role of particle phase, *Atmospheric Chem. Phys.*, 8(17), 5465–5476,  
737 doi:10.5194/acp-8-5465-2008, 2008.
- 738 Mills, P. L. and Duduković, M. P.: Deconvolution of noisy tracer response data by a linear filtering  
739 method, *AIChE J.*, 34(10), 1752–1756, doi:10.1002/aic.690341025, 1988.
- 740 Nozière, B., Barnes, I. and Becker, K.-H.: Product study and mechanisms of the reactions of  $\alpha$ -  
741 pinene and of pinonaldehyde with OH radicals, *J. Geophys. Res.*, 104(D19), 23645,  
742 doi:10.1029/1999JD900778, 1999.
- 743 Ortega, A. M., Day, D. A., Cubison, M. J., Brune, W. H., Bon, D., de Gouw, J. A. and Jimenez, J.  
744 L.: Secondary organic aerosol formation and primary organic aerosol oxidation from biomass-  
745 burning smoke in a flow reactor during FLAME-3, *Atmospheric Chem. Phys.*, 13(22), 11551–  
746 11571, doi:10.5194/acp-13-11551-2013, 2013.
- 747 Ortega, A. M., Hayes, P. L., Peng, Z., Palm, B. B., Hu, W., Day, D. A., Li, R., Cubison, M. J.,  
748 Brune, W. H., Graus, M., Warneke, C., Gilman, J. B., Kuster, W. C., de Gouw, J. A. and Jimenez,  
749 J. L.: Real-time measurements of secondary organic aerosol formation and aging from ambient air  
750 in an oxidation flow reactor in the Los Angeles area, *Atmospheric Chem. Phys. Discuss.*, 15(15),  
751 21907–21958, doi:10.5194/acpd-15-21907-2015, 2015.
- 752 Paulson, S. E., Pandis, S. N., Baltensperger, U., Seinfeld, J. H., Flagan, R. C., Palen, E. J., Allen,  
753 D. T., Schaffner, C., Giger, W. and Portmann, A.: Characterization of photochemical aerosols from  
754 biogenic hydrocarbons, *J. Aerosol Sci.*, 21, S245–S248, doi:10.1016/0021-8502(90)90230-U,  
755 1990.
- 756 Peng, Z., Day, D. A., Stark, H., Li, R., Lee-Taylor, J., Palm, B. B., Brune, W. H. and Jimenez, J.  
757 L.: HO<sub>x</sub> radical chemistry in oxidation flow reactors with low-pressure mercury lamps  
758 systematically examined by modeling, *Atmospheric Meas. Tech.*, 8(11), 4863–4890,  
759 doi:10.5194/amt-8-4863-2015, 2015.
- 760 Peng, Z., Day, D. A., Ortega, A. M., Palm, B. B., Hu, W., Stark, H., Li, R., Tsigaridis, K., Brune,  
761 W. H. and Jimenez, J. L.: Non-OH chemistry in oxidation flow reactors for the study of  
762 atmospheric chemistry systematically examined by modeling, *Atmospheric Chem. Phys.*, 16(7),  
763 4283–4305, doi:10.5194/acp-16-4283-2016, 2016.



- 764 Pereira, K. L., Hamilton, J. F., Rickard, A. R., Bloss, W. J., Alam, M. S., Camredon, M., Ward,  
765 M. W., Wyche, K. P., Muñoz, A., Vera, T., Vázquez, M., Borrás, E. and Ródenas, M.: Insights  
766 into the Formation and Evolution of Individual Compounds in the Particulate Phase during  
767 Aromatic Photo-Oxidation, *Environ. Sci. Technol.*, 49(22), 13168–13178,  
768 doi:10.1021/acs.est.5b03377, 2015.
- 769 Renbaum, L. H. and Smith, G. D.: Artifacts in measuring aerosol uptake kinetics: the roles of time,  
770 concentration and adsorption, *Atmospheric Chem. Phys.*, 11(14), 6881–6893, doi:10.5194/acp-11-  
771 6881-2011, 2011.
- 772 Rudich, Y., Donahue, N. M. and Mentel, T. F.: Aging of Organic Aerosol: Bridging the Gap  
773 Between Laboratory and Field Studies, *Annu. Rev. Phys. Chem.*, 58(1), 321–352,  
774 doi:10.1146/annurev.physchem.58.032806.104432, 2007.
- 775 Seinfeld, J. H. and Pandis, S. N.: *Atmospheric chemistry and physics: from air pollution to climate*  
776 *change*, 2nd ed., J. Wiley, Hoboken, N.J., 2006.
- 777 Simonen, P., Saukko, E., Karjalainen, P., Timonen, H., Bloss, M., Aakko-Saksa, P., Rönkkö, T.,  
778 Keskinen, J. and Dal Maso, M.: A New Oxidation Flow Reactor for Measuring Secondary Aerosol  
779 Formation of Rapidly Changing Emission Sources, *Atmospheric Meas. Tech. Discuss.*, 1–27,  
780 doi:10.5194/amt-2016-300, 2016.
- 781 Slowik, J. G., Wong, J. P. S. and Abbatt, J. P. D.: Real-time, controlled OH-initiated oxidation of  
782 biogenic secondary organic aerosol, *Atmospheric Chem. Phys. Discuss.*, 12(3), 8183–8224,  
783 doi:10.5194/acpd-12-8183-2012, 2012.
- 784 Smith, J. D., Kroll, J. H., Cappa, C. D., Che, D. L., Liu, C. L., Ahmed, M., Leone, S. R., Worsnop,  
785 D. R. and Wilson, K. R.: The heterogeneous reaction of hydroxyl radicals with sub-micron  
786 squalane particles: a model system for understanding the oxidative aging of ambient aerosols,  
787 *Atmospheric Chem. Phys.*, 9(9), 3209–3222, doi:10.5194/acp-9-3209-2009, 2009.
- 788 Sun, Y.: *Study on the Internal Effect of Inhibiting Gas and Solid Back-Mixing in Fluidized Beds*,  
789 Masters, Tsinghua University, Beijing., 2010.
- 790 Taylor, G.: Dispersion of Soluble Matter in Solvent Flowing Slowly through a Tube, *Proc. R. Soc.*  
791 *Math. Phys. Eng. Sci.*, 219(1137), 186–203, doi:10.1098/rspa.1953.0139, 1953.
- 792 Taylor, G.: Conditions under Which Dispersion of a Solute in a Stream of Solvent can be Used to  
793 Measure Molecular Diffusion, *Proc. R. Soc. Math. Phys. Eng. Sci.*, 225(1163), 473–477,  
794 doi:10.1098/rspa.1954.0216, 1954a.
- 795 Taylor, G. I.: Diffusion and Mass Transport in Tubes, *Proc. Phys. Soc. Sect. B*, 67(12), 857–869,  
796 doi:10.1088/0370-1301/67/12/301, 1954b.
- 797 Turpin, B. J., Saxena, P. and Andrews, E.: Measuring and simulating particulate organics in the  
798 atmosphere: problems and prospects, *Atmos. Environ.*, 34(18), 2983–3013, doi:10.1016/S1352-  
799 2310(99)00501-4, 2000.



800 Villermaux, J.: Macro and Micromixing Phenomena in Chemical Reactors, in Chemical Reactor  
801 Design and Technology, edited by H. I. Lasa, pp. 191–244, Springer Netherlands, Dordrecht.  
802 [online] Available from: [http://www.springerlink.com/index/10.1007/978-94-009-4400-8\\_6](http://www.springerlink.com/index/10.1007/978-94-009-4400-8_6)  
803 (Accessed 11 December 2015), 1986.

804 Volkamer, R., Platt, U. and Wirtz, K.: Primary and Secondary Glyoxal Formation from Aromatics:  
805 Experimental Evidence for the Bicycloalkyl–Radical Pathway from Benzene, Toluene, and *p* -  
806 Xylene, J. Phys. Chem. A, 105(33), 7865–7874, doi:10.1021/jp010152w, 2001.

807 Went, F. W.: Blue Hazes in the Atmosphere, Nature, 187(4738), 641–643, doi:10.1038/187641a0,  
808 1960.

809 Williams, B. J., Goldstein, A. H., Kreisberg, N. M. and Hering, S. V.: An In-Situ Instrument for  
810 Speciated Organic Composition of Atmospheric Aerosols: Thermal Desorption Aerosol GC/MS-  
811 FID (TAG), Aerosol Sci. Technol., 40(8), 627–638, doi:10.1080/02786820600754631, 2006.

812 Zhao, Y., Kreisberg, N. M., Worton, D. R., Teng, A. P., Hering, S. V. and Goldstein, A. H.:  
813 Development of an *In Situ* Thermal Desorption Gas Chromatography Instrument for Quantifying  
814 Atmospheric Semi-Volatile Organic Compounds, Aerosol Sci. Technol., 47(3), 258–266,  
815 doi:10.1080/02786826.2012.747673, 2013.

816 Zwietering, T. N.: The degree of mixing in continuous flow systems, Chem. Eng. Sci., 11(1), 1–  
817 15, doi:10.1016/0009-2509(59)80068-3, 1959.

818

819

820

821

822